THE JOURNAL OF PHYSICAL CHEMISTRY C

ARTICLE

pubs.acs.org/JPCC

Low-Temperature Synthesis and Characterization of Gallium Nitride Quantum Dots in Ordered Mesoporous Silica

Konstantinos Dimos,[*,†,‡] L'uboš Jankovič,[†,§] Ioannis B. Koutselas,[*,‡] Michael A. Karakassides,[†] Radek Zbořil,[∥] and Peter Komadel[§]

[†]Department of Materials Science and Engineering, University of Ioannina, GR-45110 Ioannina, Greece

[‡]Department of Materials Science, University of Patras, GR-26504 Patras, Greece

[§]Institute of Inorganic Chemistry, Slovak Academy of Sciences, Dúbravská cesta 9, SK-84536 Bratislava, Slovakia

[∥]Regional Centre of Advanced Technologies and Materials, Faculty of Science, Department of Physical Chemistry, Palacký University in Olomouc, CZ-77146 Olomouc, Czech Republic

Supporting Information

ABSTRACT: Semiconducting gallium nitride (GaN) quantum dots (QDs) were synthesized at low temperatures (650 °C), using ammonia flow without any organogallium precursor compound, assisted and controlled by an ordered mesoporous silica MCM-41 as host matrix. The final materials exhibit an intense blue shift of the band gap energy compared to the three-dimensional (3D) GaN. MCM-41 hosted GaN QD synthesis is also reported from pyrolysis of an organic precursor, tris(dimethylamido)-gallium(III), at 365 °C under ammonia flow, with the largest band gap blue shift reported for such synthesized GaN of 0.6 eV. The QDs, involving inorganic precursor, exhibit an average X-ray diffraction estimated diameter of 12.6 Å and crystallize in the zinc blende lattice with cubic symmetry (β-GaN), whereas the hexagonal system is thermodynamically preferred. QDs, based on organic precursor, have hexagonal symmetry (α-GaN, wurtzite structure) with an average diameter of 20.6 Å. Spectroscopic and structural characterization of the QD-MCM composites showed the successful synthesis of well-defined distributions of QDs, exhibiting luminescence at high energies in the UV region and in some cases defect luminescence, depending on the specific synthetic route.

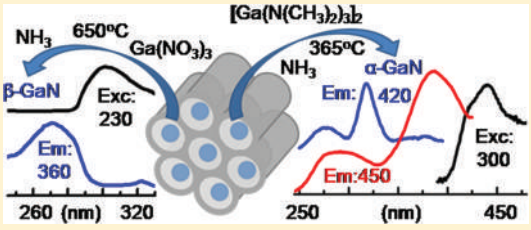

1. INTRODUCTION

Semiconducting materials have attracted the scientific community's attention over the past decades as these set the basis for computational engineering, microelectronics, optical devices, light-emitting diodes, and more recently photovoltaic systems.[1−3] One of the most popular semiconductors that is being extensively studied due to its unique properties is gallium nitride (GaN).

GaN is a direct III−V wide-gap semiconductor with either hexagonal symmetry (α-GaN), wurtzite structure with a three-dimensional (3D) energy gap (E_g) of E_{g3D} = 3.4 eV (365 nm), or cubic symmetry (β-GaN) acquired with zinc blende structure and E_{g3D} = 3.2 eV (387 nm);[4,5] however, crystallization in the zinc blende lattice is rarely observed.[6] GaN is an important semiconductor due to its large energy direct band gap and chemical stability and has found numerous applications, as for example in blue-light-emitting diode, ultraviolet photodetectors, photocatalyst in photoelectrochemical cells, high-temperature electronic devices, and others.[7−9]

Nanotechnology, encompassing a multitude of synthetic and analytic advanced techniques, has lately led to the successful synthesis and study of a new class of materials, many of which have semiconducting character, possessing confined dimensionality for the electrons and holes, which will be referred to as low-dimensional (LD) semiconductors. These systems may have one, two, or three restricted dimensions forming quantum two-dimensional (2D) wells (QW), quantum one-dimensional (1D) wires (QWi), or quantum zero-dimensional (0D) dots (QDs), respectively.[10] LD semiconductors exhibit exotic and unique properties compared to their relative 3D systems, due to the quantum confinement effects, which manifest strongly when the electronic restriction is comparable or even smaller than the Bohr's exciton radius of the specific semiconductor.[11−13] In these LD semiconductors, the band gap is increased as well as the excitonic binding energy and excitonic oscillator strength, in the progression of shifting from 3D to 2D, 1D, and finally 0D systems. The novel enhanced optical properties of these LD systems along with the semiconducting character of the nanoparticles makes them in fact novel future materials for optoelectronic applications,[14,15] and this has been the case for LD GaN systems which have been synthesized over the past years with such properties.[4,16−20]

Synthesis of LD semiconductors can be achieved with a variety of methods such as chemical synthesis, epitaxial methods, or

Received: August 19, 2011
Revised: December 7, 2011
Published: December 07, 2011

ordered molecular self-assembly in various environments, which can be distinguished by the chemistry routes, the cost, the final form, and energy consumption. In this case a combination of chemistry within confined active mesoporous space is being implemented.[7,16]

In a parallel field of modern research of synthetic mesoporous materials, materials of the M41S family have been developed and have been used for a range of applications.[21,22] MCM-41 is defined as ordered silica mesoporous molecular sieve, analogous to the aluminosilicate zeolites. It is the best known and studied M41S family member and is composed of hexagonal arrays of well-oriented mesopores, interspaced with SiO_2 walls, exhibiting large surface area. MCM-41 has been used as a selective sorbent,[23−27] stereoselective heterogeneous catalyst,[28,29] molecular sieve for gas separation,[30,31] and a matrix for growth control, etc.[32,33] MCM-41 has 3−4.5 mequiv of OH^-/g and is in this work capable of binding cations such as Ga^{3+}.[34−36] Due to its chemical nature, this porous quartz materials class can host a multitude of reactions or physical phenomena and restrict the dimensionality of the reaction pathways as well as the final products.

During previous years various synthetic procedures for 0D, 1D, 2D, or 3D GaN materials production have been applied. Nevertheless, the vast majority of these procedures are based either on expensive and dangerous organogallium precursors[4,17,18,37−39] or on highly energetic techniques, since GaN is normally formed at high temperatures,[40] while its direct synthesis from Ga and N is highly exothermic, leading to extreme local heating and possible decomposition.[41] It must be mentioned that catalyst-based methods can reduce the required synthesis temperature.[39]

In the present work, we report the synthesis of LD GaN QDs in a mesoporous silicate matrix (MCM-41) with a common inorganic (nitrate) gallium salt at low temperatures (650 °C), as well as the preparation of luminescent GaN QDs within the MCM-41 matrix using organic precursors. In both experiments, the catalytic action of MCM-41 in combination with its restricted pore diameter assists the formation of GaN QDs at low temperatures even without the need of an organo-gallium precursor. On the other hand, the same catalytic capability has allowed the formation of quite small luminescent organic precursor QDs, for which it has now been possible to decrease their size even more than in reported works[17,38] and retain a relatively intense high-energy, defect-based, luminescence than previously reported.

2. EXPERIMENTAL SECTION

2.1. Materials. All materials were reagent or analytical grade and were used as purchased without further purification. Tetraethylorthosiilicate (TEOS, 98%) was purchased from Sigma-Aldrich, aqueous ammonia solution (NH_3, 25 wt %) from Fluka, cetyltrimethylammonium bromide (CTAB, 95%) from Sigma-Aldrich, ethanol (EtOH, 99.5%) from Panreac, gallium nitrate hydrate ($Ga(NO_3)_3 \cdot H_2O$, 99.9%) from Sigma-Aldrich, and gaseous ammonia (100%) from Aeroscopio Hellas. For the sample with the precursor the following have also been used: trioctylamine ($[CH_3(CH_2)_7]_3N$, 98+%) from Fluka, tris(dimethylamido)-gallium(III) ($[Ga(N(CH_3)_2)_3]_2$, 98%) from Sigma-Aldrich, and *N*,*N*-dimethylformamide (DMF, 99+%) from Merck.

2.2. Synthesis. The MCM-41 sample was synthesized by hydrolyzing 50 g of TEOS, added in a 1 L polyethylene bottle containing 417.5 g of H_2O, 268.5 g of NH_3 (25 wt %), and 10.5 g of CTAB. Each of the previous additions was stirred for 30 min. The product was retrieved after heat treatment at 80 °C for 96 h, which can be slightly considered as hydrothermal treatment. It was filtered, rinsed with cold ethanol (EtOH), and finally placed on a plate for air-drying (sample, MCM-41). For comparison reasons, a heat-treated sample was also prepared for which 200 mg of MCM-41 was heated at 550 °C for 5 h with a 2 °C/min heating rate (sample, HT⊗MCM-41). A 300 mg amount of MCM-41 was treated with 280 mg of $Ga(NO_3)_3 \cdot H_2O$ in 36 mL of EtOH for 35 min at 70 °C. The product was then centrifuged and rinsed with cold EtOH, and afterward the isolated precipitate was re-dispersed in 30 mL of EtOH. A 140 mg amount of $Ga(NO_3)_3 \cdot H_2O$ was added for the same treatment at 70 °C for 15 min, followed by centrifugation and rinsing with cold EtOH. Next, the product was placed on a plate for air-drying (sample, Ga⊗MCM-41). A 100 mg amount of Ga⊗MCM-41 was placed in a porcelain crucible-boat inside a tubular furnace and was heat-treated at 650 °C for 5 h with a 2 °C/min heating rate under continuous ammonia flow. Ammonia flow was maintained until the sample reached room temperature (RT) again (sample, GaN⊗MCM-41).

For the gallium nitride QDs prepared with organic precursor the following reaction was performed under nitrogen atmosphere inside a glovebox. A 500 mg amount of MCM-41, which had been evacuated at 300 °C for 24 h (sample, 300⊗MCM-41), was dispersed in 25 mL of trioctylamine in a 100 mL spherical flask, followed by 5 min of stirring. Then 500 mg of tris-(dimethylamido)gallium(III) was added, and the flask was transferred in a heating mantle. The reaction took place at 365 °C for 4 h under continuous ammonia flow of about 1 mL/s. Ammonia flow was maintained until the solution reached room temperature again, and the solid product was isolated by centrifugation. Sediment was re-dispersed in DMF and centrifuged, and this procedure was repeated three times. Finally, the sample was placed on a plate for air-drying at RT (sample, GaN_d⊗MCM-41).

2.3. Characterization. X-ray powder diffraction (XRD) data were collected on a D8 Advance Bruker diffractometer using Cu Kα (40 kV, 40 mA, λ = 1.541 78 Å) radiation and a secondary beam graphite monochromator. Diffraction patterns were collected in the 2θ range from 2 to 80°, in steps of 0.02° and 2 s counting time/step.

Peak fitting in the wide-angle X-ray powder diffraction patterns was performed using the WinSpec 2.09 peak fitting program. In practice we have chosen the minimum number of peaks that give reasonable agreement between experimental and calculated patterns. Peaks were assumed to have mixed (Gaussian/Lorentzian) profile since this line shape gave the optimum fit.

Infrared spectra were measured on a Perkin-Elmer GX, Fourier transform spectrometer in the frequency range of 400−4000 cm^{-1}. Samples were pulverized and dispersed in KBr, from which compacted pellets were used for recording the spectra, an average of 64 scans at 2 cm^{-1} resolution.

The nitrogen adsorption−desorption isotherms were measured at 77 K on a Sorptomatic 1990, Thermo Finnigan porosimeter. Specific surface areas S_{BET} were determined with the Brunauer−Emmett−Teller (BET) method using adsorption data points in the relative pressure P/P_0 range of 0.01−0.30. The desorption branches of the isotherms were used for the pore size calculations according to the Kelvin equation $r_k \sim 4.146/(\log(P_0/P))$ (Å), where P_0 is the saturated vapor pressure in

equilibrium with the adsorbate condensed in a capillary or a pore, P is the vapor pressure of a liquid contained in a cylindrical capillary, and r_k is the Kelvin radius of the capillary or pore. The Kelvin equation was used according to the Barrett−Joyner−Halenda (BJH) method for calculation of core radii and the pore size distribution (PSD) of the samples. All samples used for the surface analyses were outgassed at 150 °C for 16 h under high vacuum (10^{-5} mbar) before the measurements.

Thermogravimetric (TG) analysis and differential thermal analysis (DTA) were performed using a Perkin-Elmer Pyris Diamond TG/DTA Instruments. Samples of approximately 5 mg were heated in air from 25 to 900 °C, with a 5 °C/min rate.

Scanning electron microscopy (SEM) images were taken using a JEOL JSM-5600 scanning electron microscope. Energy dispersive X-ray spectra (EDS) were also collected. The EDS analysis results were the average of five different regions of surface measurements of each sample. EDS analyses were also compared with those obtained from an EVO-MA10 Carl Zeiss scanning electron microscope.

Transmission electron microscopy (TEM) observations were performed on a JEOL JEM-2010 transmission electron microscope equipped with LaB_6 cathode (accelerating voltage of 200 kV; point-to-point resolution of 0.194 nm). A drop of high-purity distilled water, containing the ultrasonically dispersed particles, was placed onto a Holey Carbon film supported by a copper-mesh TEM grid and air-dried at room temperature.

UV−vis spectra were recorded on a Shimadzu UV-2401PC two-beam spectrophotometer in the range of 200−800 nm, at a step of 0.5 nm, using a combination of deuterium and halogen lamps as sources. The presented spectra were obtained from thin film deposits transmission. These have also been confirmed to be the same as those obtained from diffuse reflectance experiments of solid pressed pellets, through the Kubelka−Monk relation.

The PL spectra were obtained from solid pressed pellets mounted in a Jobin Yvon Fluorolog 3 spectrofluorometer FL-11 employing a xenon 450 W lamp and a P928P photodetector. Slits were set at 4 nm spectral resolution. The photoluminescence excitation and emission spectra have been corrected through the instrument supplied files, created from compounds with known quantum yields and an included Si photodetector. All optical UV−vis and PL spectra were recorded at room temperature.

3. RESULTS AND DISCUSSION

3.1. Structural Characterization. X-ray powder diffraction patterns in the low-angle region of the samples MCM-41, Ga⊗MCM-41, and GaN⊗MCM-41 are shown in Figure 1. The first two are typical of MCM-41 materials with the characteristic strong reflection at low scattering angles 2θ and hexagonal arrangement of uniform pores. MCM-41 is classified in the *P6mm* space group, which means that the first reflection peak is attributed to the Miller (100) lattice planes. Specifically, the XRD pattern of sample MCM-41 (Figure 1a) displays four reflection peaks corresponding to the d_{100}, d_{110}, d_{200}, and d_{210} spacings. The fact that even the d_{210} spacing reflection is observed indicates that the hexagonal arrangement of the pores in the pristine material is maintained in a wide range. Applying Bragg's law for the first reflection peak leads to d_{100} spacing of 41.0 Å. The pattern in Figure 1b of sample Ga⊗MCM-41 shows the first three reflection peaks with a d_{100} spacing of 39.9 Å,

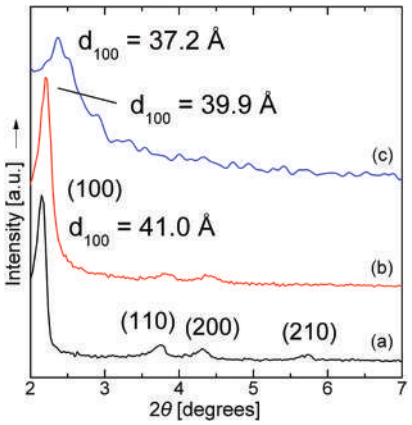

Figure 1. X-ray powder diffraction patterns in the low-angle region for the MCM-41 matrix for samples MCM-41 (a), Ga⊗MCM-41 (b), and GaN⊗MCM-41 (c).

suggesting a small shrinkage in the pore diameters in spite of maintaining the wide-range hexagonal pore ordering.

Hexagonal arrangement is, however, missing in the pattern of the final product in Figure 1c. Instead, a broad d_{100} reflection peak is observed corresponding to a 37.2 Å spacing. This indicates that ammonia treatment at 650 °C partly altered the pores and disordered their wide range arrangement, though, without destroying the basic local mesopore structure of MCM-41. Moreover, filling of the pores with gallium nitride may obstruct the diffraction of X-rays from the silicate matrix. Small structural damage to the MCM-41 matrix has negligible effect on the effort to use the catalytic advantage of MCM-41 and its narrow pore diameter distribution in order to assist and control the development of GaN nanoparticles at low temperatures. Should the MCM-41 structure need to be retained, then treatment with ammonia at lower temperatures and/or for shorter time would be a solution, however, resulting in more complex properties of GaN due to possible byproduct reactants being produced.

Additionally, X-ray powder diffraction patterns in the low-angle region of samples in all stages of the precursor originated QDs synthesis, denoted as MCM-41, 300⊗MCM-41, and GaN_d⊗MCM-41, are shown in Figure 2. The spectrum in Figure 2a is identical with the one in Figure 1a, since the same starting MCM-41 material was used in both cases. The pattern in Figure 2b of sample 300⊗MCM-41 exhibits all four main reflection peaks with a d_{100} spacing of 39.5 Å, suggesting a small shrinkage in the pore diameters in spite of maintaining the wide-range hexagonal pore ordering. Last, in Figure 2c, it is evidenced that in the sample GaN_d⊗MCM-41—unlike the organo-free-derived sample—the wide-range hexagonal pore structure of the MCM-41 matrix is maintained, as the (110) and (200) originated reflection peaks are present and the main (100) peak is narrow enough with a corresponding d_{100} spacing of 39.6 Å. In fact, this value is very close to the spacing of sample 300⊗MCM-41, indicating that the final ammonia heat treatment did not affect the matrix.

Figure 3 shows the X-ray powder diffraction pattern in the 2θ scattering angle region of 15−44° of GaN⊗MCM-41 (the pattern in the whole angle region of 10−80° is available in the Supporting Information in Figure S1). As it can be observed, the XRD pattern in this region exhibits two dominant reflection

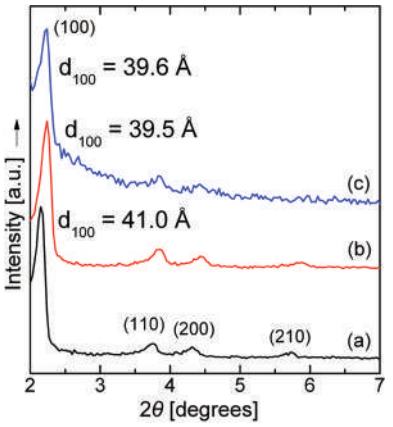

Figure 2. X-ray powder diffraction patterns in the low-angle region for the MCM-41 matrix for samples MCM-41 (a), 300⊗MCM-41 (b), and GaN_d⊗MCM-41 (c).

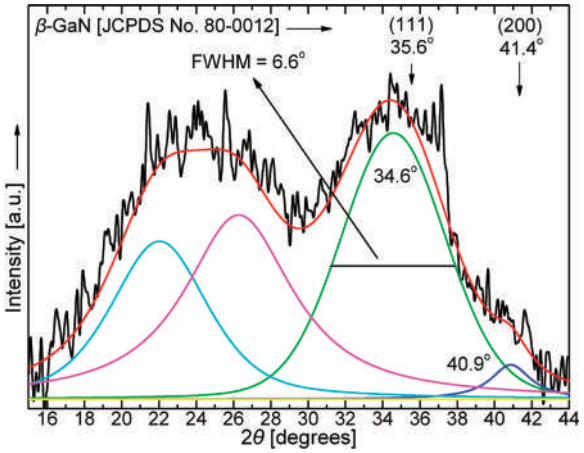

Figure 3. Wide-angle X-ray powder diffraction pattern of GaN⊗MCM-41.

peaks, the first from ∼17 to ∼30° and the second from ∼30 to ∼40°, as well as a small shoulder around 41°. A multipeak fitting, performed as presented in the Experimental Section, reveals four broad peaks (with error bar at ca. 1° for the full width at half-maximum (fwhm), corresponding to ∼4 Å uncertainty for the diameter size). The first two peaks present also in the patterns of samples MCM-41 and Ga⊗MCM-41 are attributed to the amorphous silicate wall structure of MCM-41 (patterns available in the Supporting Information in Figure S3), while the third peak at 34.6°, observed only in sample GaN⊗MCM-41, is attributed to the (111) lattice planes of the zinc blende β-GaN phase [JCPDS No. 80-0012]. Because wurtzite hexagonal symmetry (α-GaN) is thermodynamically preferred and more common, the probability of crystallization in this lattice structure was also considered and multipeak mixed Gaussian/Lorentzian profile curve fittings were performed. However, it has not been feasible for any realistic fit parameter set to correlate to the data because α-GaN has three reflection peaks from (100), (002), and (101) lattice planes at the same angle region and, thus, the α form does not exist. Moreover, the fourth peak at 40.9° is attributed to the (200) lattice planes of β-GaN, while α-GaN does not exhibit any reflection peaks in this region. This fact confirms the above claim about the formation of β-GaN instead of the more stable α-GaN.

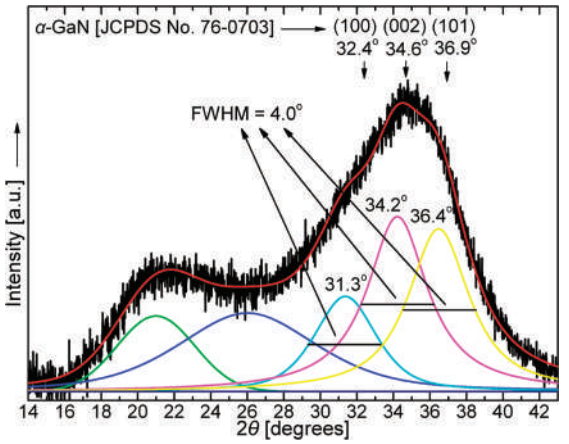

Figure 4. Wide-angle X-ray powder diffraction pattern of GaN_d⊗MCM-41.

In this conclusion we are also led by the absence of any shoulder at about 31−32° in GaN⊗MCM-41's pattern (Figure 3), verifying that indeed gallium nitride in sample GaN⊗MCM-41 possesses the not so common zinc blende symmetry. The average size (D_{hkl}) of the formed β-GaN nanoparticles can be estimated from the fwhm of the (111) diffraction peak (6.6°) using Scherrer's equation[42] and is estimated to be 12.6 Å. This size is nearly half of the exciton Bohr radius which is ca. 25 Å,[4] which implies that the formed gallium nitride nanoparticles show quantum effects and will exhibit analogous optoelectronic properties, as reported below.

In contrast, sample GaN_d⊗MCM-41, presented in Figure 4 and prepared as reported by Mićić et al.,[4] obviously crystallizes with hexagonal symmetry. The main difference between these two diffraction patterns (Figures 3 and 4) is the fact that in the pattern of sample GaN_d⊗MCM-41 in the same angle region (∼30 to ∼40°) a multipeak fit in the second dominant reflection peak is more appropriate as distinguishable shoulders at ∼31−32° and ∼36−37° are present. The curve fitting resulted in five broad peaks (with error bar at ca. 1° for the fwhm, corresponding to ∼4 Å uncertainty for the diameter size). As mentioned previously, the first two peaks are assigned to the amorphous silicate wall structure of MCM-41, while the next three at 31.3, 34.2, and 36.4° are attributed to peaks originating from the (100), (002), and (101) lattice planes of the wurtzite α-GaN phase [JCPDS No. 76-0703]. The average size (D_{hkl}) of the formed α-GaN nanoparticles is again estimated with Scherrer's equation[42] at about 20.6 Å, close to the exciton Bohr radius. This estimated value along with the optoelectronic properties presented further on can be correlated with the shape of the formed QDs as discussed later.

Figure 5 shows the Fourier transform infrared spectra of samples MCM-41, Ga⊗MCM-41, and GaN⊗MCM-41. The spectrum in Figure 5a of pristine MCM-41 exhibits absorption peaks at ν_{max}: 462, 801, 960, 1079, and 1238 cm^{-1} that are attributed to inorganic silicate matrix vibrations. Specifically, peaks are assigned as follows: 462 s ρ(Si−O−Si), 801 m δ(Si−O−Si), 960 w ν_{asym}(Si−OH), 1079 vs ν_{asym}(Si−O−Si) transverse-optical mode, and 1238 m ν_{asym}(Si−O−Si) longitudinal-optical mode.[34] Additional peaks are assigned as 1487 w $\delta(CH_2)$, 2855 s $\nu_{sym}(CH_2)$, 2926 s $\nu_{asym}(CH_2)$, and 1643 w $\delta(H_2O)$.

The spectrum in Figure 5b has the same silicate peaks, a stronger 1643 br $\delta(H_2O)$ peak and an additional 3473 br $\nu(H_2O)$ peak. There are two main differences between these

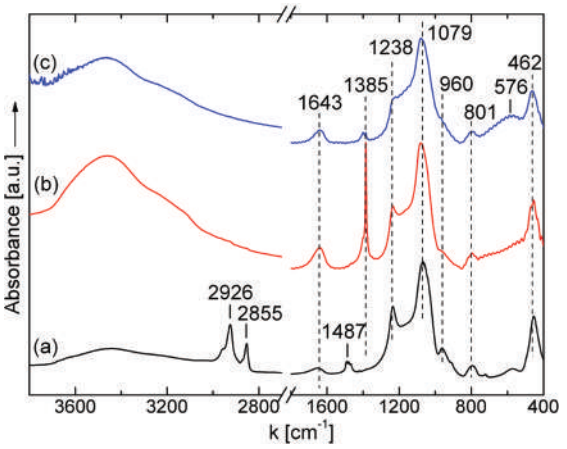

Figure 5. FT-infrared spectra of MCM-41 (a), Ga⊗MCM-41 (b), and GaN⊗MCM-41 (c).

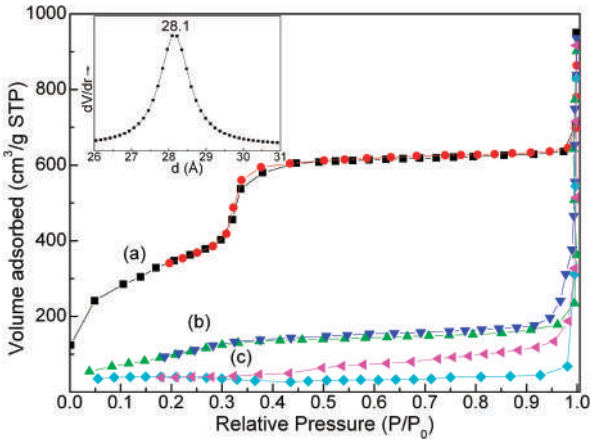

Figure 6. Nitrogen adsorption−desorption isotherms for HT⊗MCM-41 (a), Ga⊗MCM-41 (b), and GaN⊗MCM-41 (c). Inset: pore distribution calculated from N_2 desorption branch for sample HT⊗MCM-41.

two spectra. First, the lack of organic attributed peaks in the spectrum of Figure 5b indicates the complete successful removal of the surfactant molecules. Second, the additional peak at 1385 cm^{-1}, due to double degenerate antisymmetric N−O stretching vibrations of NO_3^- ions, confirms the substitution of the template by $Ga(NO_3)_3 \cdot H_2O$ after the ion-exchange reactions in EtOH, as NO_3^- are also inserted as compensating anions. The above differences denote also that Ga^{3+} cations are uniformly grafted almost exclusively onto the MCM-41 surface of the internal walls as the extracted surfactant molecules were inside the pores and the majority of the receptor Si−O$^-$ groups are mainly located in the internal walls since it is known that only 5−10% of the total specific surface area of MCM-41 materials is attributed to external surfaces.[32,34] The spectrum in Figure 5c of the final sample GaN⊗MCM-41 has common silicate and H_2O originated peaks with the previous spectra as well as two significant differences compared to the spectrum of Figure 5b. The 1385 cm^{-1} peak is nearly completely vanished as NO_3^- groups are forced to leave the pores and a new broad peak at 576 cm^{-1} arises. This new peak is assigned to the transverse-optical lattice phonon mode of GaN nanocrystals.[40,43] The appearance of this peak in spectrum Figure 5c, while being absent in Figure 5b, confirms GaN development after ammonia treatment. The same peak is also evidenced in the spectrum of sample GaN_d⊗MCM-41 (not presented here), indicating GaN formation in this sample, too.

The nitrogen adsorption−desorption isotherms of samples HT⊗MCM-41, Ga⊗MCM-41, and GaN⊗MCM-41 and the pore size distribution curve of sample HT⊗MCM-41, in the inset, are both shown in Figure 6, as Figure 6a−c respectively. As mentioned in the experimental part, sample HT⊗MCM-41 was prepared only for additional information about the parent MCM-41 material. Its isotherm (Figure 6a) is categorized as type IV classification,[44] which is characteristic of MCM-41 mesoporous materials adsorption. The presence of a sharp sorption step in the adsorption curve, at P/P_0 at about 0.33, indicates that the sample possesses a well-defined array of regular mesopores. The specific surface area was calculated using BET equation and was found to be 1280 m^2/g.[45,46] The desorption branch was used to calculate the mesopore size distribution by means of the Barrett−Joyner−Halenda (BJH) method.[47] From the PSD curve of the HT⊗MCM-41 sample (Figure 6 inset) its mean pore diameter was calculated at about 28.1 Å. These data suggest that the other samples, all well-defined mesopores and similarly synthesized, should exhibit slightly bigger mean pore diameter since heat treatment shrinks the pores.[32,34] The isotherm (Figure 6b) of the Ga⊗MCM-41 sample significantly differs from its corresponding previous isotherm (Figure 6a). Although, it is type IV as well, no sharp sorption step is observed. This, in combination with X-ray diffraction results, means that even if the hexagonal arrangement is maintained as concluded by X-rays, the sample seems to lack uniform mesopores and a narrow pore size distribution. However, it is more possible that filling of the mesopores with gallium nitrate from the ion-exchange reactions influences and changes the relative pressure that pores absorb, making it impossible to estimate a pore size distribution curve by the BJH method. Specific surface area was calculated using the BET equation and was found to be 407 m^2/g. This value verifies that the pores are to a large extent filled by gallium nitrate. The isotherm of Figure 6c is similar to the one of Figure 6b. No sharp sorption step is observed as expected on the basis of the isotherm of its origin sample (Ga⊗MCM-41), and in addition no PSD curve was estimated. The iIsotherm has a large hysteresis loop, while from BET theory the specific surface area was calculated to be equal to 130 m^2/g. This value is low enough for MCM-41 materials which indicates that pores in the final GaN⊗MCM-41 sample are filled with gallium nitride nanoparticles. The isotherm of sample GaN_d⊗MCM-41 (not presented here) is like the ones of Figure 6b,c. With use of the BET equation, the specific surface area was calculated to be equal to 234 m^2/g and everything mentioned about the two previous samples is valid for this one too.

Thermal DTA/TG diagrams of the GaN⊗MCM-41 sample under oxygen flow are shown in Figure 7. It is observed that nanocomposite material is thermodynamically stable up to 650 °C. The DTA signal has no peaks except probably two, almost untraceable, exothermic shoulders at 180 and 250 °C which are accompanied by a very small weight loss of about ∼2%. This loss is possibly linked with combustion of organic traces that had remained in the sample. Sample loss up to 650 °C is only ∼8%, which is expected as the silicate matrix and the formed gallium nitride are stable materials. Above 650 °C the sample shows a slight weight gain of about ∼1%, without a corresponding peak in the DTA signal. This is attributed to gradual oxidation

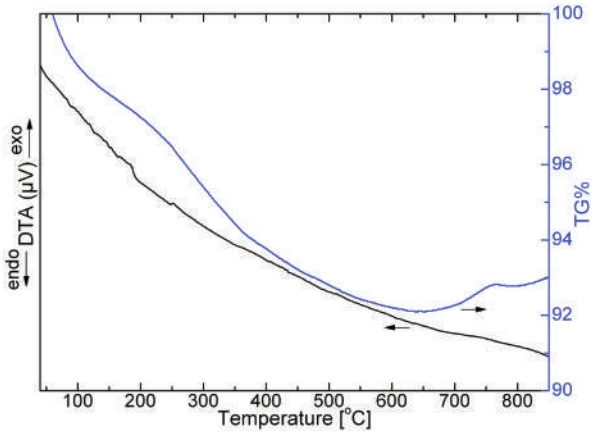

Figure 7. DTA/TG diagrams of the GaN⊗MCM-41 sample.

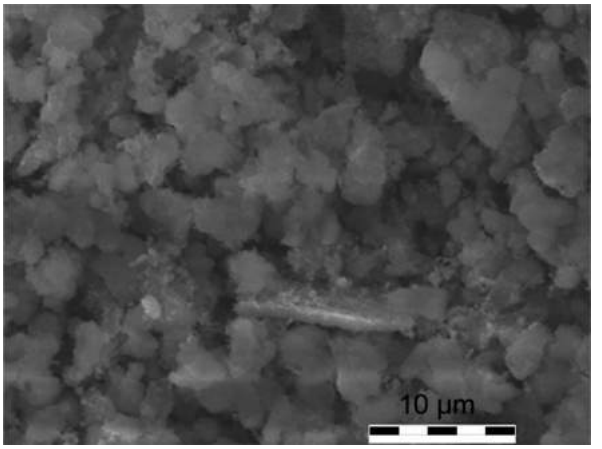

Figure 8. SEM image of GaN⊗MCM-41.

and conversion of GaN to Ga_2O_3, which terminates at higher temperatures.[48] The previous conclusion is also confirmed by the fact that this increase is not observed when thermal analysis is carried out under nitrogen flow.[49,50]

Representative SEM and TEM images of the final GaN⊗MCM-41 sample are shown in Figures 8 and 9, respectively. SEM images do not reveal detailed information about the sample except a general morphological characterization. The sample consists of MCM-41 particles and clusters mostly of irregular shapes with a mean diameter of about 4−6 μm. The TEM image shows a small ~50 × 50 nm region of the sample in which the silicate MCM-41 matrix and some darker spots which correspond to GaN nanoparticles inside the filled pores are seen. As it is observed, there are no formed large GaN clusters outside the pores confirming the aforementioned X-ray powder diffraction results.

EDS microanalysis results indicate that sample GaN⊗MCM-41 is composed of 16% atomic Ga (41.9 wt %) and 13.1% atomic N (6.9 wt %). This means that the stoichiometric ratio of Ga/N is about 1.2/1, suggesting that there are nitrogen vacancy defects in the final sample, while the loading (~50 wt %) is very high, confirming the pores' filling suggested by the porosity measurements. Also, because GaN crystal outer surfaces are usually Ga-rich,[51] this is a fact that will be more pronounced in the GaN nanocrystals and could account for small nonstoichiometric results; however, there is

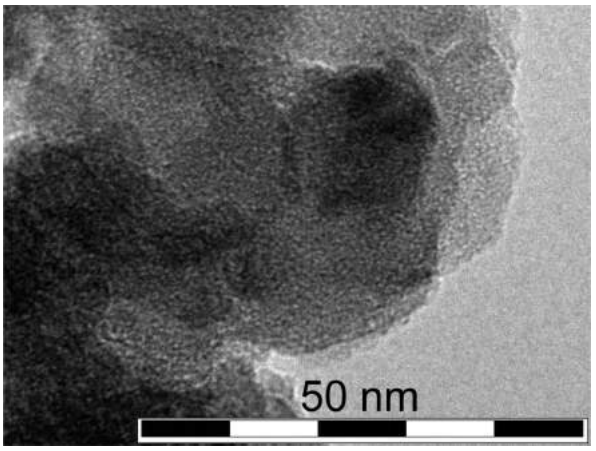

Figure 9. TEM image of GaN⊗MCM-41.

no reason that prohibits both occurring simultaneously in the formed nanoparticles. EDS analysis results support the optoelectronic properties of the sample GaN⊗MCM-41 reported later. The same microanalysis on GaN_d⊗MCM-41, averaged in a much larger extent of the sample surface, showed that it consists of 22.3% atomic Ga (50.2 wt %) and 4.5% atomic N (2 wt %). The stoichiometric ratio of Ga/N of about 5 suggests that there is significant number of nitrogen vacancy defects in the final sample or that there is a small percentage of the organoprecursor that has not completely decomposed, or some gallium oxynitrides have formed, although this would have required higher temperatures. Also, in the case of the more severe heated gallium nitrate samples, oxynitride formation is not expected.[52] Such oxynitride phases have not been detected with optical absorption spectroscopy which would have low energy band gap, ca. 2.2−2.8 eV or otherwise, except for the possible bonding of Si−O−N, which however, appears at the same frequency, in the infrared, with the hydroxyl group.[53] Again, EDS results support the optoelectronic properties presented later.

3.2. Optoelectronic Properties. UV−vis optical absorption (OA) spectra of samples Ga⊗MCM-41 and GaN⊗MCM-41 are shown in Figure 10a,b, respectively. It is evident, from spectrum Figure 10b, that the final sample exhibits a broad absorption peak below 355 nm, absent in the other absorption spectrum (Figure.10a). This broad peak can only be attributed to absorption from the formed semiconducting β-GaN nanoparticles, also confirming the results from characterization techniques presented above. The small absorbance gradient at high wavelengths is believed to be due to scattering effects. As aforementioned, the energy gap of 3D β-GaN is 3.2 eV (387 nm), suggesting that the formed nanoparticles are LD and have at least a 32 nm band gap "blue-shift" with respect to the 3D compound. The broadness of the absorption leads to two not necessarily exclusive reasons that either (i) nanoparticles formed have a broad size distribution or (ii) these are much smaller than those whose energy gap corresponds to 355 nm but exhibit defects that appear as absorbing states within the band gap. These defects would have to relate to Ga or N dislocations or deficiencies. The estimated particle size of 12.6 Å is derived from Scherrer's equation using X-ray powder diffraction, and, thus, such size implies a high probability of surface structural defects. It must be noted that the defects cannot originate from massive O_2 reaction with Ga as there is no evidence of gallium oxide, also semiconductor, in the XRD spectra, but EDS analysis supports that the nonstoichiometric correspondence

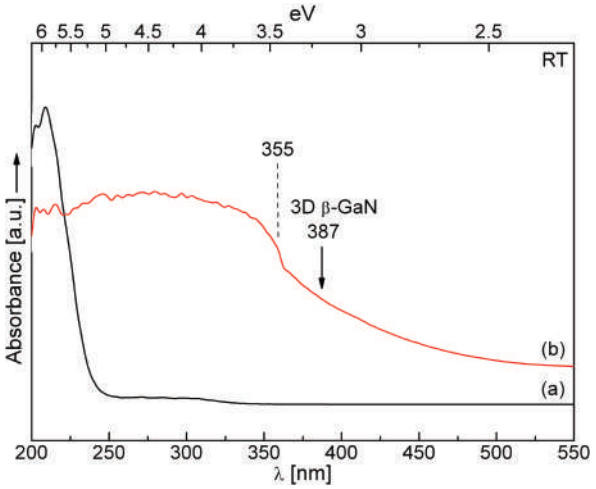

Figure 10. Absorbance spectra of samples Ga⊗MCM-41 (a) and GaN⊗MCM-41 (b).

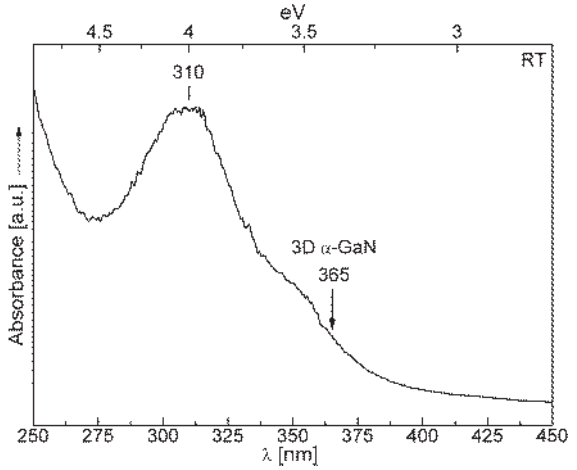

Figure 11. Absorbance spectrum of sample GaN_d⊗MCM-41.

of Ga to N may indeed lead to structural defects. Defect-related optical properties have been discussed in various contexts and methods, i.e., can enhance band edge photoluminescence in GaN materials,[54,55] leading also to yellow/green luminescence.[56,57] More information about the optoelectronic properties of the sample can be deduced with photoluminescence (PL) emission and excitation (PLE) spectroscopy, as described further on, and will yield information about the exact position of the band gap.

In Figure 11, the GaN_d⊗MCM-41 absorption spectrum at room temperature is presented. It is observed that there is a distinct intense peak at 310 nm and a shoulder at 355 nm, denoting the formation of a rather monodisperse QD type, which shows at least a 55 nm band gap blue shift, and a second phase of QDs that have only a 10 nm blue shift, when compared to the 3D α-GaN, of E_{g3D} at 365 nm. From the absorbance peak area, after baseline correction, it is suggested that the majority of the nanoparticles should be those whose size corresponds to a band gap of 310 nm. Such GaN quantum dots, prepared from organic precursor at low temperatures, were never reported before. Finally, the small increase of absorbance from 400 nm toward lower wavelengths is due to scattering effects.

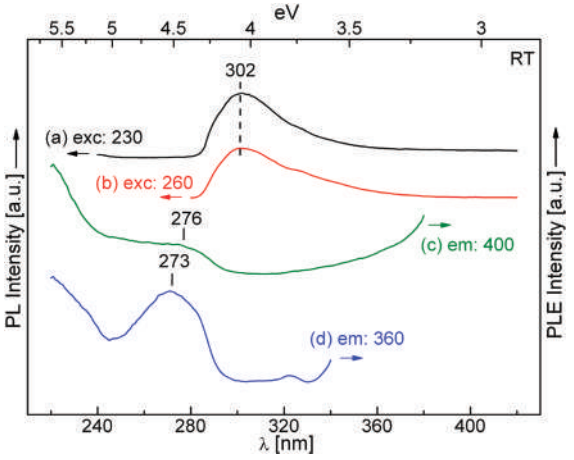

Figure 12. PL (left) and PLE (right) spectra of GaN⊗MCM-41 (a, excitation at 230 nm; b, excitation at 260 nm; c, emission at 400 nm; d, emission at 360 nm).

Figure 12 shows the PL (left) and PLE (right) spectra of GaN⊗MCM-41 at room-temperature: (a) excitation at 230 nm, (b) excitation at 260 nm, (c) emission at 400 nm, and (d) emission at 360 nm. Spectra a and b have the same emission peak at 302 nm (4.1 eV) despite the different excitation wavelengths, suggesting an electron recombination mechanism at this energy which is either due to the band gap or an impurity/defect state within the band gap, and thus, it can be assumed that the band gap is at least 4.1 eV and in this case, both OA and PL would be strongly due to defects. As it was discussed before, the defect-related PL at low energies, ca. 440 and 525 nm, have been discussed by various authors in various contexts,[56,57] but it is important to note the here-reported distinct peak appearance instead of a broad convoluted low energy peak as in reference 17. PLE spectra c and d, despite their different emission wavelengths, exhibit nearly the same peak at ca. 275 nm (4.5 eV), while spectrum d shows also a small peak at 322 nm. The peaks at ca. 275 nm are not believed to be a single peak but seem to be two Gaussian peaks, the most important at 280 nm, but are discussed for simplicity as one. Actually, when λ_{em} = 360 nm, where the OA absorbance step is found, the PLE 273 nm peak becomes intense, as λ_{em} is closer to the state giving rise to the 360 nm emission. Also, the 320 nm peak in Figure 12d is intense when λ_{em} = 360 nm. These imply that the main absorption peaks leading to considerable luminescence are located at 275 (4.5 eV) and 322 nm, and their convolution is thought to create the broad peak in Figure 10b. The PLE peak at 320 nm is considered responsible for the broad asymmetry of PL peaks at 320 nm, of Figure 12a,b, and the PLE 273 nm peak is responsible for giving Stokes-shifted photoluminescence at the 302 nm peaks of Figure 12a,b. It is not considered that the PLE peak centered at 275 nm is related to some defect introduced into the MCM matrix after the GaN synthesis, since if this were the case, the PLE spectra would have to exhibit distinct peaks, different from the 275 nm peaks, responsible for the 302 nm PL peak. Energy-transfer phenomena between nanoparticles could also be a partial reason for the broadness/asymmetry of the PL peaks, as energy can be absorbed and emitted at different nanoparticles, slowly losing energy at each transfer. Knowing that the energy gap of 3D β-GaN is 3.2 eV, we could conclude that nanoparticles demonstrate a band gap blue shift of 1.3 eV. For completion, reference

dx.doi.org/10.1021/jp208011y |J. Phys. Chem. C 2012, 116, 1185–1194

PL/PLE spectra, found in the Supporting Information, have been measured for undoped and calcined MCM-41 showing that there are PL peaks at uncorrelated wavelength positions to the here-reported data, of smaller intensity and shifting depending on the excitation energy, e.g., the λ_{exc} = 230 nm peak at 345 nm and the λ_{exc} = 260 nm peak at 318 nm. Moreover, HT⊗MCM-41 PLE reference spectra show a low-intensity peak at 365 nm and small shoulder on the Rayleigh scattering at 285 nm. In all cases, the reference host MCM-41 spectra show that the reported PL spectral data are not related to the MCM-41 matrix.

It is a fact that, under specific circumstances and assumptions, analytical equations can associate the energy gap with the geometrical size in a LD system. So, from the PL/PLE data we can estimate a radius of a spherical GaN quantum dot with the above optoelectronic properties by using eq 1, which is known as Brus' active mass model.[58−62]

$$\Delta E = \frac{h^2}{8\mu R^2} - 1.786\frac{e^2}{4\pi\varepsilon_{QD}\varepsilon_o R} \quad (1)$$

In eq 1, ΔE is the blue shift of the energy gap in joules ($(1.3 \times 1.602) \times 10^{-19}$ J), h is Planck's constant (6.626×10^{-34} J·s), μ is the reduced mass of the electron/hole pair, R is the estimated radius in meters, e is the electron's charge (1.602×10^{-19} C), π is the Archimedes constant (~3.14), ε_{QD} is the static dielectric constant of nanoparticles, and ε_o is the vacuum dielectric constant (8.854×10^{-12} F·m^{-1}). For the calculation of μ for the formed β-GaN nanoparticles the following values have been selected: m_e = 0.13 m_0 and m_{hh} = 1.3 m_0 (where m_e and m_{hh} are active masses of electron and heavy hole, respectively, and m_0 is electrons' rest mass equal to 9.1095×10^{-31} kg).

For ε_{QD} a size-dependent expression (eq 2) has been used since the static dielectric constant of a LD nanoparticle differs significantly from the dielectric constant of its 3D material (ε_{3D}).[63]

$$\varepsilon_{QD} = 1 + \frac{\varepsilon_{3D} - 1}{1 + (\Delta E^2/E_g{}^2)} \quad (2)$$

In eq 2, ε_{3D} is 9.7 (zinc blende) and 8.9 (wurtzite), ΔE = 1.3 eV, and E_g is the energy gap equal to 4.5 eV. Solving these equations, it is concluded that the spherical β-GaN quantum dots with the previous optoelectronic properties should have a radius of ca. 14.6 Å (particle diameter, 29.2 Å), varying on the order of 0.1 nm for different choices of dielectric constants. This calculated value is significantly bigger than the estimated particle size with Scherrer's equation by X-ray diffraction pattern (D_{hkl} = 12.6 Å), a value which is a minimum bound to the average particle size in a particular crystallographic direction.

However, this difference between the two values does not imply the inexactness of either of the two methods. This is because the LD nanoparticles are formed inside MCM-41's cylindrical mesopores and they are restricted in a way to eventually form nanowires due to the matrix. This implies that the formed nanoparticles are not in fact faultless spheres but they rather have a cylindrical shape. In this case, Scherrer's equation gives a mean value of the two dimensions that characterize the nonspherical nanoparticles.[64] Moreover, it can be that adjacent nanoparticles behave optically as larger, and this energy transfer between them could explain this discrepancy. Unfortunately, there is not any theoretical model about anisotropic quantum dots that would equate the calculations by both Scherrer and Brus equations. On the other hand, the Brus equation is based on the optoelectronic properties and resembles these data for hypothetical spherical particle. The above suggest that the nanoparticles have indeed an average size as estimated by Scherrer's equation and can be compared with spherical quantum dots of the calculated radius by the Brus equation.[32] Finally, as aforementioned, the exciton Bohr radius of gallium nitride is ca. 25 Å; therefore, nanoparticles as reported are expected not only to show pronounced electrooptical effects but also exhibit large exciton binding energy,[65] in agreement with the observed 1/2 eV minimum energy difference between the 273 nm peak of Figure 11d and its preceding higher energy valley at 5 eV.

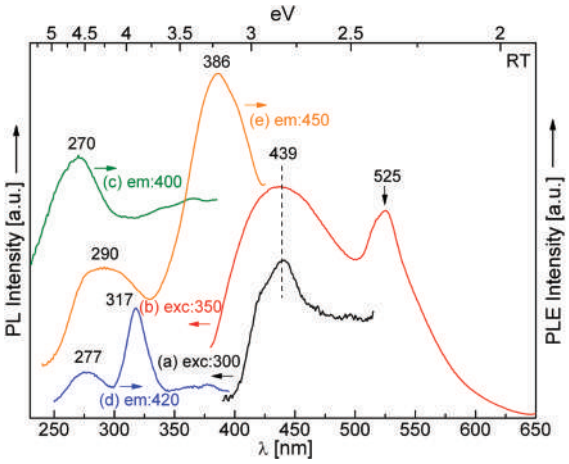

Figure 13. PL (left) and PLE (right) spectra of GaN_d⊗MCM-41 (a, excitation at 300 nm; b, excitation at 350 nm; c, emission at 400 nm; d, emission at 420 nm; e, emission at 450 nm).

On the basis of the above facts and the combination of all information by X-ray, EDS, UV−vis, and PL/PLE data, regarding the optoelectronic properties we conclude that formed β-GaN nanoparticles have an average size of 12.6 Å, E_g = 4.5 eV, displaying a 1.3 eV blue shift with respect to the relative 3D system.

Figure 13 shows the PL and PLE spectra of GaN_d⊗MCM-41: (a) excitation at 300 nm, (b) excitation at 350 nm, (c) emission at 400 nm, (d) emission at 420 nm, and (e) emission at 450 nm. PL spectra show broad emission peaks at 439 and 525 nm, which are due to pure defect luminescence, since the well-defined size distribution, evidenced by the corresponding absorption spectrum, does not allow for energy-transfer phenomena between different sized nanoparticles. On the other hand, PLE spectra exhibit peaks corresponding to absorption peaks that slightly differ depending on the emission frequency selection. In particular, when the emission wavelength is set at λ_{em} = 400 nm, then only a major contributing absorption peak at ca. 270 nm is observed, while a small shoulder appears at 360 nm. When λ_{em} is set to 420 nm, peaks at 277 and 317 nm are observed along with a small shoulder at 375 nm, while when λ_{em} = 450 nm, then a broad peak with underlying centers at 270 and 290 nm is observed along with a strong low-energy peak at 386 nm. These imply that depending on the luminescence position, various mechanisms appear that the system follows toward equilibrium and is rather impossible to explain all with a monodisperse set of quantum dots, since the high-energy PLE peak is not appearing at constant wavelength. Also, it is difficult to explain such data assuming that the nanoparticles have some of the well-known asymmetrical shapes acquired by GaN, such as pyramids. In particular,

high-energy luminescence (i.e., λ_{em} = 400 nm) can be efficiently invoked by the 270 nm state, probably because the 400 nm PL is due to the Stokes-shifted luminescence of the energy gap, located around 270 nm, corresponding to a small type of particles. In the case of the λ_{em} = 420 nm PLE spectrum, luminescence originates from absorption at 277 and 317 nm, both thought to be absorption states, however, corresponding to both the first sized set of QDs discussed and larger nanoparticles, from those responsible for the PLE spectra in Figure 13c. In the case of λ_{em} = 450 nm, the broad absorption peak covers all nanoparticles sizes yielding luminescence at 450 nm, while it also shows absorption at wavelengths much larger than hose corresponding to 3D GaN and, thus, should be related to defects absorbing and reemitting light. In summary, it is safe to conclude that all PL and PLE spectra support the formation of QD with band gap at 317 nm and a smaller set with ca. 275 nm band gap, however, showing defect luminescence at low energies. Finally, PL spectra with excitation at 250 nm also show a distinct luminescence peak at ca. 310 nm without Stokes shift compared to the absorption peak at 310 nm, included in the Supporting Information in Figure S5.

The previously used Brus' active mass model can also be applied for the GaN_d⊗MCM-41 sample; however, different values for some parameters must be used, as in this case the formed nanoparticles have wurtzite structure (α-GaN). Thus, active masses of electron and heavy hole are $m_e = 0.27\ m_0$ and $m_{hh} = 0.8\ m_0$ and the dielectric constant of its 3D material (ε_{3D}) is equal to 8.9 and E_{g3D} is taken as 3.39 eV. As a result, the estimated radius of a spherical GaN quantum dot with the above optoelectronic properties by using eqs 1 and 2 is $R \sim 11$ Å (particle diameter, 22 ± 2 Å) for assuming the 270 nm as the energy gap, while 16 Å (particle diameter, 32 ± 2 Å) for the 317 nm peak. These calculated values are close to the estimated particle size by Scherrer's equation (D_{hkl} = 20.6 Å), and all are in qualitative agreement for the case of the organic precursor. It is thought that the use of the inorganic gallium nitrate leads to a different QD morphology, affecting the size calculations.

4. CONCLUSIONS

In the present work semiconducting GaN QDs were synthesized in the MCM-41 pores at low temperatures with (i) a common inorganic (nitrate) gallium salt and (ii) an organogallium precursor. In the first case, Ga^{3+} cations were uniformly dispersed exclusively on the inner surface of the MCM-41 pores (GaN⊗MCM-41). Nanoparticles' size and dimensionality were controlled by the pore diameter of the mesoporous silicate matrix. Nanoparticles of an average diameter size of 12.6 Å with ellipsoidal geometry formed and crystallized in the zinc blende lattice (β-GaN), whereas the hexagonal system is thermodynamically preferred and more common. These exhibit an intense blue shift of ca. 1.3 eV, an excitonic luminescence peak at 302 nm, and optical properties that are in good agreement with the estimated particle size, with insignificant blue/green luminescence. For the second case (GaN_d⊗MCM-41), QDs were crystallized in the wurtzite lattice (α-GaN) and an estimated size of about 20.6 Å. The latter also exhibit an intense blue shiftof at least 0.6 eV and a well-defined UV absorption peak, and for the first time, photoluminescence at the absorption peak without Stokes shift, for the specific organic precursor used.

■ ASSOCIATED CONTENT

Supporting Information. Wide-angle X-ray powder diffraction patterns in the region of 10−80° of GaN⊗MCM-41 and GaN_d⊗MCM-41 (Figures S1 and S2, respectively) and of samples MCM-41 and Ga⊗MCM-41 (Figure S3a,b, respectively), PL and PLE spectra of HT⊗MCM-41 (Figure S4), and PL spectrum of GaN_d⊗MCM-41 with excitation at 250 nm (Figure S5). This material is available free of charge via the Internet at http://pubs.acs.org.

■ AUTHOR INFORMATION

Corresponding Author
*E-mail: kdimos@cc.uoi.gr (K.D.); ikouts@upatras.gr (I.B.K.).

■ ACKNOWLEDGMENT

The authors acknowledge financial support from the Collaboration Program of the Slovak Republic and Greece (Project No. 16: "New clay-nanosemiconductive hybrids").

■ REFERENCES

(1) Brennan, K. F. *Introduction to semiconductor devices: For computing and telecommunications applications*; Cambridge University Press: Cambridge, U.K., 2005.
(2) Fukuda, M. *Optical semiconductor devices*; John Wiley & Sons Inc.: New York, NY, USA, 1999.
(3) Luque, A.; Hegedus, S. *Handbook of photovoltaic science and engineering*; John Wiley & Sons: West Sussex, U.K., 2005.
(4) Mićić, O. I.; Ahrenkiel, S. P.; Bertram, D.; Nozik, A. J. *Appl. Phys. Lett.* **1999**, *75* (4), 478–480.
(5) Bougrov, V.; Levinshtein, M. E.; Rumyantsev, S. L.; Zubrilov, A. *Properties of advanced semiconductor materials: GaN, AlN, InN, BN, SiC, SiGe*; John Wiley & Sons: New York, NY, USA, 2001.
(6) Vurgaftman, I.; Meyer, J. R.; Ram-Mohan, L. R. *J. Appl. Phys.* **2001**, *89* (11), 5815–5875.
(7) Pankove, J. I. *GaN and related materials*; Gordon and Breach: Amsterdam, The Netherlands, 1997.
(8) Qiu, C. H.; Melton, W.; Leksono, M. W.; Pankove, J. I.; Keller, D. P.; Baars, S. P. D. *Appl. Phys. Lett.* **1996**, *69* (9), 1282–1284.
(9) Morkoç, H.; Strite, S.; Gao, G. B.; Lin, M. E.; Sverdlov, B.; Burns, M. *J. Appl. Phys.* **1994**, *76* (3), 1363–1398.
(10) Green, M.; O'Brien, P. *Chem. Commun. (Cambridge, U. K.)* **1999**, 2235–2241.
(11) Papavassiliou, G. C. *Solid State Chem.* **1981**, *40* (3), 330–335.
(12) Berry, C. R. *Phys. Rev.* **1967**, *161*, 848–851.
(13) Ekimov, A. I.; Onuschchenko, A. A.; Tsekhomskii, V. A. *Fiz. Khim. Stekla* **1980**, *6* (4), 511–512.
(14) Koutselas, I.; Bampoulis, P.; Maratou, E.; Evagelinou, T.; Pagona, G.; Papavassiliou, G. C. *J. Phys. Chem. C* **2011**, *115*, 8475–8483.
(15) Jankovič, L.; Dimos, K.; Bujdák, J.; Koutselas, I. B.; Madejová, J.; Gournis, D.; Karakassides, M. A.; Komadel, P. *Phys. Chem. Chem. Phys.* **2010**, *12*, 14236–14244.
(16) Gil, B. *Low-dimensional nitride semiconductors*; Oxford University Press: New York, NY, USA, 2002.
(17) Winkler, H.; Birkner, A.; Hagen, V.; Wolf, I.; Schmechel, R.; Seggern, H. V.; Fischer, R. A. *Adv. Mater.* **1999**, *11* (17), 1444–1448.
(18) Kim, Y. H.; Lee, J. Y.; Lee, S.-H.; Oh, J.-E.; Lee, H. S. *Appl. Phys. A: Mater. Sci. Process.* **2005**, *80*, 1635–1639.
(19) Li, Z. J.; Chen, X. L.; Li, H. J.; Tu, Q. Y.; Yang, Z.; Xu, Y. P.; Hu, B. Q. *Appl. Phys. A: Mater. Sci. Process.* **2001**, *72*, 629–632.
(20) Li, L.; Shi, J.-L. *Nanotechnology* **2006**, *17*, 344–348.
(21) Kresge, C. T.; Leonowicz, M. E.; Roth, W. J.; Vartuli, J. C.; Beck, J. S. *Nature* **1992**, *359* (6397), 710–712.

(22) Beck, J. S.; Vartuli, J. C.; Roth, W. J.; Leonowicz, M. E.; Kresge, C. T.; Schmitt, K. D.; Chu, C. T. W.; Olson, D. H.; Sheppard, E. W.; McCullen, S. B.; Higgins, J. B.; Schlenker, J. L. *J. Am. Chem. Soc.* **1992**, *114*, 10834–10843.
(23) Vartuli, J. C.; Malek, A.; Roth, W. J.; Kresge, C. T.; McCullen, S. B. *Microporous Mesoporous Mater.* **2001**, *44*−*45*, 691–695.
(24) Xu, Y. M.; Wang, R. S.; Wu, F. *J. Colloid Interface Sci.* **1999**, *209*, 380–385.
(25) Huang, L.; Xiao, H.; Ni, Y. *Colloids Surf., A* **2004**, *247*, 129–136.
(26) Algarra, M.; Jiménez, M. V.; Castellón, E. R.; López, A. J.; Jiménez, J. J. *Chemosphere* **2005**, *59*, 779–786.
(27) Stathi, P.; Dimos, K.; Karakassides, M. A.; Deligiannakis, Y. *J. Colloid Interface Sci.* **2010**, *343*, 374–380.
(28) Taguchi, A.; Schüth, F. *Microporous Mesoporous Mater.* **2005**, *77*, 1–45.
(29) Corma, A. *Chem. Rev.* **1997**, *97*, 2373–2420.
(30) Øye, G.; Sjöblom, J.; Stöcker, M. *Adv. Colloid Interface Sci.* **2001**, *89*−*90*, 439–466.
(31) Xu, X.; Song, C.; Miller, B. G.; Scaroni, A. W. *Fuel Process. Technol.* **2005**, *86* (14−15), 1457–1472.
(32) Dimos, K.; Koutselas, I. B.; Karakassides, M. A. *J. Phys. Chem. B* **2006**, *110*, 22339–22345.
(33) Zhang, J.; Han, B.; Hou, Z.; Liu, Z.; He, Z.; Jiang, T. *Langmuir* **2003**, *19*, 7616–7620.
(34) Dimos, K.; Stathi, P.; Karakassides, M. A.; Deligiannakis, Y. *Microporous Mesoporous Mater.* **2009**, *126*, 65–71.
(35) Kumar, D.; Schumacher, K.; Hohenesche, C. D. F. V.; Grün, M.; Unger, K. K. *Colloids Surf., A* **2001**, *187*−*188*, 109–116.
(36) Zhao, X. S.; Lu, G. Q.; Whittaker, A. K.; Millar, G. J.; Zhu, H. Y. *J. Phys. Chem. B* **1997**, *101*, 6525–6531.
(37) Frank, A. C.; Fischer, R. A. *Adv. Mater.* **1998**, *10* (12), 961–964.
(38) Winkler, H.; Devi, A.; Manz, A.; Wohlfart, A.; Rogge, W.; Fischer, R. A. *Phys. Status Solidi A* **2000**, *177*, 27–35.
(39) Chang, K.-W.; Wu, J.-J. *J. Phys. Chem. B* **2002**, *106*, 7796–7799.
(40) Qiu, H.; Cao, C.; Zhu, H. *Mater. Sci. Eng., B* **2007**, *136*, 33–36.
(41) Wang, J.; Grocholl, L.; Gillan, E. G. *Nano Lett.* **2002**, *2*, 899–902.
(42) Guinier, A. *X-ray diffraction in crystals, imperfect crystals, and amorphous bodies*; Dover: New York, NY, USA, 1994.
(43) Ng, S. S.; Hassan, Z.; Haslim, M. R.; Kordesch, M. E. *Mater. Chem. Phys.* **2005**, *91*, 404–408.
(44) Sing, K. S. W.; Everett, D. H.; Haul, R. A. W.; Moscou, L.; Pierotti, R. A.; Rouquerol, J.; Siemieniewska, T. *Pure Appl. Chem.* **1985**, *57*, 603–619.
(45) Brunauer, S.; Emmett, P. H.; Teller, E. *J. Am. Chem. Soc.* **1938**, *60*, 309–319.
(46) Bhambhani, M. R.; Cutting, P. A.; Sing, K. S. W.; Turk, D. H. *J. Colloid Interface Sci.* **1972**, *38* (1), 109–117.
(47) Barrett, E. P.; Joyner, L. G.; Halenda, P. P. *J. Am. Chem. Soc.* **1951**, *73*, 373–380.
(48) Xiao, H.-D.; Ma, H.-L.; Xue, C.-S.; Zhuang, H.-Z.; Ma, J.; Zong, F.-J.; Hu, W.-R. *Mater. Lett.* **2005**, *59*, 4041–4043.
(49) Song, Y. T.; Wu, X.; Wang, W. J.; Yuan, W. X.; Chen, X. L. *J. Alloys Compd.* **2004**, *370*, 65–68.
(50) Xiao, H.-D.; Ma, H.-L.; Lin, Z.-J.; Ma, J.; Zong, F.-J.; Zhang, X.-J. *Mater. Chem. Phys.* **2007**, *106*, 5–7.
(51) Zywietz, T. K.; Neugebauer, J.; Scheffler, M. *Appl. Phys. Lett.* **1999**, *74*, 1695–1697.
(52) Sinha, G.; Panda, S. K.; Mishra, P.; Ganguli, D.; Chaudhuri, S. *J. Phys.: Condens. Matter* **2007**, *19*, No. 346209(1−10).
(53) Hu, C.-C.; Teng, H. *J. Phys. Chem. C* **2010**, *114*, 20100–20106.
(54) Schwenzer, B.; Hu, J.; Seshadri, R.; Keller, S.; DenBaars, S. P.; Mishra, U. K. *Chem. Mater.* **2004**, *16*, 5088–5095.
(55) Jung, W.-S.; Park, C.; Han, S. *Bull. Korean Chem. Soc.* **2003**, *24*, 1011–1013.
(56) Reshchikov, M. A.; Morkoç, H. *Physica B* **2006**, *376*−*377*, 428–431.
(57) Gai, L.; Jiang, H.; Ma, W.; Cui, D.; Lun, N.; Wang, Q. *J. Phys. Chem. C* **2007**, *111*, 2386–2390.
(58) Yin, J. X.; Yan, J.; Zhi-lin, Z.; Xu, S.-H. *J. Cryst. Growth* **1998**, *191* (4), 692–696.
(59) Denzler, D.; Olschewski, M.; Sattler, K. *J. Appl. Phys.* **1998**, *84*, 2841–2845.
(60) Brus, L. E. *J. Chem. Phys.* **1984**, *80*, 4403–4409.
(61) Brus, L. *J. Phys. Chem.* **1986**, *90*, 2555–2560.
(62) Kayanuma, Y. *Phys. Rev. B* **1988**, *38*, 9797–9805.
(63) Tsu, R.; Babic, D.; Loriatti, L., Jr. *J. Appl. Phys.* **1997**, *82*, 1327–1329.
(64) Kumpf, C.; Neder, R. B.; Niederdraenk, F.; Luczak, P.; Stahl, A.; Scheuermann, M.; Joshi, S.; Kulkarni, S. K.; Barglik-Chory, C.; Heske, C.; Umbach, E. *J. Chem. Phys.* **2005**, *123* (22), 224707–224712.
(65) Ramvall, P.; Riblet, P.; Nomura, S.; Aoyagi, Y.; Tanaka, S. *J. Appl. Phys.* **2000**, *87* (8), 3883–3890.